

Recent Advances in Atomic Timekeeping: Optical Clocks

Greg Smith*

Department of Physics, Ohio State University, Columbus, OH 43210

(Dated: June 24, 2014)

Introduction

Motivation for Precise Timekeeping

A recent paper [1] reports an atomic clock that is accurate and stable at the 10^{-18} level¹. One might wonder why society would need a such a good clock. To put this unprecedented level of stability into perspective, consider that it would take roughly the age of the universe for this clock to gain or lose one second. Although not useful for everyday timekeeping, such a clock has important scientific applications. It can be used to perform improved measurements of the fine structure constant α and the Rydberg constant R_∞ (including searching for time variation of these constants) [2–5]. Since they are sensitive enough to detect gravity-induced time dilation, clock-based geodesy (using frequency shifts to map out gravitational fields) will become a possibility [1, 5]. Comparing clocks based on the 1S-2S transitions in hydrogen and anti-hydrogen could provide precision tests of the fundamental symmetry between matter and anti-matter [6]. The technological applications of a 10^{-18} clock are presently unclear, but they may arise in the future. This was the case for Cs-based clocks prior to their use in the Global Positioning System [6].

This paper will discuss the latest improvement in ^{87}Sr optical lattice atomic clocks: accurately correcting the so-called *black-body radiation (BBR) shift*. As discussed below, this is the dominant systematic error (fractional frequency shift) present in optical lattice clocks. They determined the BBR shift of their clock to be $-4,962.9(1.8) \times 10^{-18}$, resulting in an overall shift of $-5,921.2(6.4) \times 10^{-18}$. This uncertainty (6.4×10^{-18}) is currently the lowest reported systematic uncertainty² reported in a clock [1]. Before getting into the details of this experiment, we will first discuss some basic facts about atomic clocks. Then, we will discuss the relevant strontium electronic structure that makes a ^{87}Sr clock possible and outline the theory of BBR shifts. Calculation of the BBR shift requires knowledge of the differential atomic polarizability $\Delta\alpha$ between the upper and lower clock states in strontium, which was recently measured with unprecedented accuracy [7]. Finally, we will discuss how this new measurement has been applied to improve the ^{87}Sr optical lattice atomic clocks at JILA.

¹ Unless otherwise noted, all uncertainties in this paper will be reported as relative uncertainties.

² This *uncertainty* will become *accuracy* once the SI second is redefined.

What Exactly is an Atomic Clock?

The principle behind an atomic clock is not so different from that of a simple grandfather clock (see Fig. 1). The pendulum in a grandfather clock is calibrated so that the period (and thus the frequency) of the pendulum's oscillation is known relative to the second. For each oscillation, a mechanical device coupled to the pendulum advances a set of gears by an appropriate amount, and this change is reflected by the movement of the clock's hands. Thus, a simple clock consists of two main components: a periodic source of known frequency (i.e., clock *ticks*) and a way of counting and displaying each tick [4]. Rather than use a swinging pendulum, atomic clocks use a stable laser cavity as an oscillator. The frequency of the laser is locked to the transition between two non-degenerate atomic states.³ Frequency combs are used to 'count' the ticks of optical clocks by converting the fast optical frequencies into more manageable frequencies [6].

Octave-spanning femtosecond frequency combs are arguably the most important technological piece of the optical clock puzzle. A frequency comb is a source of light whose spectrum consists of equally-spaced lines [9], as shown in Fig. 1. The frequency combs used by optical clocks are created by Kerr-lens mode-locked Ti:sapphire lasers. A frequency comb in the time-domain is a pulsed laser of repetition rate f_r , pulse duration τ and carrier-envelope phase ϕ_{ce} . In the frequency domain, this becomes a Dirac-comb-like signal with comb lines at frequencies $\nu_n = nf_r + f_0$, where n is an integer and f_0 is the offset frequency. The repetition rate f_r is easily measured by conventional means, and both f_0 and the absolute optical frequency of a cw laser can be measured in the following manner. If the frequency of the unknown laser ν_s lies close to some ν_n , then the second harmonic of the cw laser $2\nu_s$ will lie close to ν_{2n} . Heterodyning ν_s and ν_n yields the beat frequency $f_{beat1} = \nu_s - (nf_r + f_0)$; heterodyning $2\nu_s$ and ν_{2n} yields $f_{beat2} = 2\nu_s - (2nf_r + f_0)$. Then $f_{beat2} - 2f_{beat1} = f_0$. Furthermore, mixing the two beat signals will yield $f_{beat2} - f_{beat1} = \nu_s - nf_r$. The mode order n can be determined by varying f_r and repeating the measurement; thus determining the frequency of the cw laser [10].

Atoms are good candidates for frequency standards, since they have well-defined transition frequencies and abundant identical copies are readily available [12]. In theory, any two clocks locked to the same unperturbed atomic transition should keep identical time [5]. In practice, there are many sources of frequency shifts and systematic uncertainties [1]. Proper isolation of the atoms

³ In the SI system, the second is defined as the duration of 9,192,631,770 periods of the radiation corresponding to the transition between two hyperfine levels of the ground state of the cesium-133 atom. This definition refers to a cesium atom at rest at a temperature of 0 K, to account for BBR shifts [8].

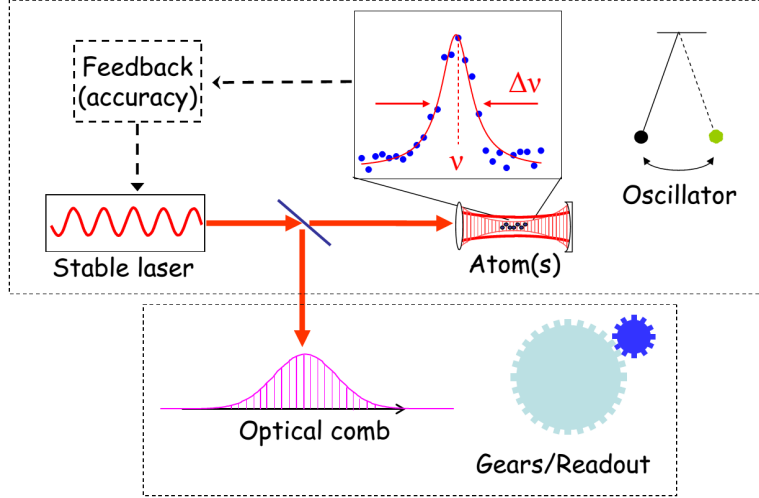


Figure 1. A clock consists of an oscillator and a readout. An optical atomic clock uses a stable laser cavity as an oscillator; the frequency of this cavity is tuned to an atomic transition. An optical frequency comb is used to determine the frequency of the laser cavity relative to a microwave frequency standard. Adapted from [11].

from the outside environment and a clever experimental design will reduce or eliminate many of these effects. The remaining frequency shifts must be accurately quantified and corrected in order to improve the clock's accuracy.

Accuracy and Stability

Stability is a measure of how a clock's frequency of oscillations changes over time; a stable clock is a consistent one. No clock may make measurements better than the statistical precision set by its instability [12]. Stability is often quoted in terms of the *Allan deviation* $\sigma_y = \left[\frac{1}{2(M-1)} \sum_{k=1}^{M-1} (y_{k+1} - y_k)^2 \right]^{1/2}$, which quantifies the frequency deviation $y_{k+1} - y_k$ between successive measurements [13]. The Allan deviation is used instead of the standard deviation formula, $\sigma = \left[\frac{1}{(M-1)} \sum_{k=1}^M (y_k - \bar{y})^2 \right]^{1/2}$, which compares each frequency measurement y_k to the global average \bar{y} , since it is less sensitive to slow drifts of the signal [14]. Sources of instability are both technical (laser instability, fluctuation in the number of atoms being probed, photon shot noise) and fundamental (quantum projection noise, discussed below) [15]. A clock becomes inaccurate if there are systematic effects (i.e., sources of frequency shifts) that change the transition frequency from its unperturbed value. Good stability is required to evaluate systematic errors in a

clock's accuracy [5].

Quantum Projection Noise (QPN)

Recent advances in laser stability and atom cooling have suppressed the technical instability to the point where quantum instability becomes important [1, 4, 12, 16]. There is a fundamental limit on clock stability, called the *quantum projection noise* (QPN), which arises from the indeterministic nature of quantum mechanics [14]. To understand the origin of QPN, consider how the transition frequency is determined: an ensemble of atoms is excited with radiation of some frequency, and then the population of the excited state is somehow measured.⁴ The exact shape of the excitation population vs frequency curve depends on the method of interrogation, but in general it will be peaked about the transition frequency, as in Fig. 8. There is no sensitivity to detuning at resonance since the slope of the curve is zero at this point; better sensitivity can be obtained by using the steeply sloped sides of the peak. When probed off-resonance, however, the atom is in a superposition of the ground state and the excited state. The quantum projection noise is a result of the non-zero variance of the number of atoms in the excited state when probed off-resonance.

Consider the situation that is relevant for an optical lattice clock, where an ensemble of N atoms is interrogated with Rabi spectroscopy to determine their transition frequency ν_0 that has an experimental linewidth γ . The time between frequency measurements is T and the results of many measurements are averaged over a time $\tau > T$. The quantum projection noise for this clock is [13]

$$\sigma_{QPN}(\tau) = \frac{\gamma}{\pi\nu_0} \sqrt{\frac{T}{N\tau}}. \quad (1)$$

The factor of $1/\sqrt{N}$ is due to the fact that probing N non-interacting atoms is equivalent to probing one atom N times; the factor of $\sqrt{T/\tau}$ has a similar origin. With all other factors being equal, a good clock has a narrow linewidth γ , a high transition frequency ν_0 , and uses a large number of atoms N . The QPN for clocks based on optical transitions is much lower than the QPN for clocks based on microwave transitions, since optical frequencies are roughly 10^5 times higher than microwave frequencies. Thus, optical atomic clocks are potentially much more stable than their microwave counterparts [4, 17]. Until recently, it wasn't possible to accurately measure these optical frequencies, but advances in femtosecond frequency combs have made it possible to compare optical and microwave frequencies [6].

⁴ The experimental details of Rabi interrogation will be described in a later section.

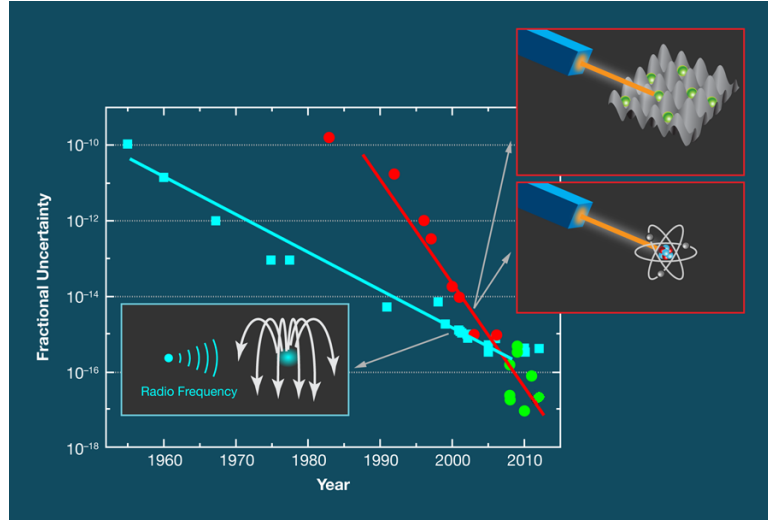


Figure 2. A timeline for atomic clock frequency uncertainty. Blue points are Cs-based microwave clocks; red and green points are optical clocks. Green points indicate clocks with uncertainties better than the microwave clocks that currently define the SI second. Adapted from [18].

A Brief History of Time(keeping)

Cesium microwave⁵ atomic clocks have been around since 1952, and their stability has increased by roughly an order of magnitude per decade (see Fig. 2). The National Bureau of Standards (NBS), now the National Institute of Standards and Technology (NIST), has played a major role in design and development of these clocks [19]. The first six designs (imaginatively named NBS-1 through NBS-6) were used as frequency standards from 1959-1993. Here, a thermal beam of ^{133}Cs ($I = 7/2$) would be state selected with a pair of magnets, then pass through two microwave cavities designed to excite the atom between two hyperfine states before passing through a second pair of magnets for state detection. Typical interaction times were on the order of 10 ms, and the observed transition linewidths were typically between 300 and 30 Hz. These designs were hindered by their passive state selection and detection schemes, which resulted in low signal to noise. In the 1990's, NIST-7 took over as the primary frequency standard. It replaced the magnets with lasers for state selection and detection, resulting in an increased signal to noise. Even so, the accuracy of NIST-7 was limited by the high velocities of a thermal beam design, which broaden the linewidths and reduce the interaction times.

In 1998, NIST-F1 became the national frequency standard [19]. It utilizes a fountain design,

⁵ The transition frequency of a microwave clock is in the microwave region of the electromagnetic spectrum.

where $\sim 10^8$ Cs atoms are laser cooled to $0.5 \mu\text{K}$ and trapped in a 1 cm^3 region. The ball of atoms is propelled upwards by a laser through a microwave cavity. The atoms reach apogee about 1 m above the cavity, then free-fall through it again on the way down. The interaction time is now ~ 1 s, with a linewidth of ~ 1 Hz. Three things limit the accuracy of this clock to the 10^{-16} level: a density shift from having a large number of atoms in a small region, a BBR shift from having the chamber walls at room temperature, and the relatively low frequency of the microwave transition. There are plans to build a second fountain clock (NIST-F2), which will overcome the first two limitations described here. However, it will still operate at microwave frequencies.

In an optical⁶ lattice clock, thousands of cold ($T \sim$ a few μK) neutral atoms are trapped in an optical lattice. The lattice wavelength is chosen such that the Stark shift (which is responsible for holding the atoms in the lattice) of the ground state and the clock state are exactly the same. This wavelength is called the *magic wavelength*, since it enables pseudo-Stark shift-free spectroscopy of the clock transition [20, 21]. Conceptually, the lattice can be thought of as many harmonic potentials. Then it is clear that the lattice will quantize the atom's harmonic oscillator (motional) states. In addition to exciting an electron to another electronic state, photons can also excite the atom to a different motional state. Thus, extra peaks (sidebands) appear on the spectrum. The stronger the atom is confined within the lattice, the further these motional sidebands are from the electronic peak of interest. The strength of the lattice confinement is characterized by the dimensionless *Lamb-Dicke parameter* $\eta = \sqrt{\nu_r/\nu_{\text{trap}}}$, where $\nu_r = \hbar k^2/2m$ is the photon recoil frequency and ν_{trap} is the lattice trap frequency [22]. Optical clocks operate in the strongly confined *Lamb-Dicke regime* ($\eta < 1$), where only two sidebands are allowed and they are well separated from the electronic peak [11, 13].

Requirements on the Atom

When choosing a transition for a clock, there should be a high probability of finding the atom in the desired state. Thus, the transition should involve the ground state. As we've seen in Eq. (1), the clock transition should have a narrow linewidth γ , which is equivalent to having a long lifetime $\Gamma \propto 1/2\pi\gamma$. The states should also be relatively insensitive to stray magnetic fields, so J should be zero for each state. To reduce Doppler effects, the atom should have a narrow transition that enables low temperature cooling. Finally, the frequencies of all relevant transitions should be

⁶ The transition frequency of an optical clock is in the optical region of the electromagnetic spectrum.

accessible by current laser technology [23].

The alkaline earth atoms (in the second column of the periodic table) have a narrow $^1S_0 - ^3P_1$ transition that can be exploited to cool down to μK temperatures. In addition, ^{87}Sr has an even narrower $^1S_0 - ^3P_0$ intercombination transition at $\nu_0 = 4.29 \times 10^{14} \text{ Hz}$ ($\lambda = 698 \text{ nm}$) with a natural linewidth $\gamma \sim 1 \text{ mHz}$ (lifetime $\Gamma \sim 150 \text{ sec}$). As discussed below, this transition is only possible in fermionic strontium [24].

Mixing of States & Forbidden Transitions in ^{87}Sr

Strontium is an alkaline earth metal with an atomic number $Z = 38$. As such, its ground state electronic configuration is $[Kr]5s^2$, with two electrons in its valence shell. There are several naturally occurring atomic isotopes, but only two are relevant for this discussion: ^{88}Sr with nuclear spin $I = 0$, and ^{87}Sr with $I = 9/2$. While ^{87}Sr is the isotope used in Ye's clock [1], its large nuclear spin complicates the electronic structure of the atom. So we will start by describing the simpler structure of ^{88}Sr before discussing the hyperfine interaction in ^{87}Sr .

As a multi-electron atom, strontium cannot be solved exactly [25]. The standard approach to this problem is perturbation theory. The main contribution to the Hamiltonian is from the electron-nucleus Coulomb interaction and the kinetic energy of the electrons. Smaller contributions come from the electron-electron Coulomb interaction, the spin-orbit interaction, and the hyperfine interaction (^{87}Sr only). For atoms with small Z , the electron-electron Coulomb interaction dominates over the spin-orbit interaction, and thus the spin-orbit interaction can be neglected. This is important because the operators⁷ \hat{L}_z , \hat{S}_z , $\hat{J}_z = \hat{L}_z + \hat{S}_z$, \hat{S}^2 , \hat{L}^2 and \hat{J}^2 all commute with the electron-electron Coulomb term, $\sum_{i>j} e^2/4\pi\epsilon_0 r_{ij}$. Thus, the quantum numbers L , S and J are good quantum numbers to describe a system without spin-orbit effects. It is convenient to describe such a system using Russel-Saunders term symbols $^{2S+1}L_J$. This is called the LS -coupling scheme, since L and S are used to describe the wavefunction.

The most important states for a ^{87}Sr clock are shown in Fig. 3. We will refer to 1S_0 as the *ground state*, 1P_1 as the *first cooling state*, 3P_1 as the *second cooling state*, and 3P_0 as the *clock state*. The states 3P_2 and 3S_1 (not shown) are useful intermediate states for cooling and population measurements. First, consider the transition $^1S_0 - ^1P_1$. This corresponds to $\Delta S = 0$, $\Delta L = 1$ and

⁷ Here, we adopt the convention for an operator or quantum number that a lower case letter is for a single electron, and a capital letter is for all valence electrons i . For a quantum number, this means $L = \sum_i l_i$ and for an operator,

$$\hat{L}_z = \sum_i \hat{l}_{z,i}.$$

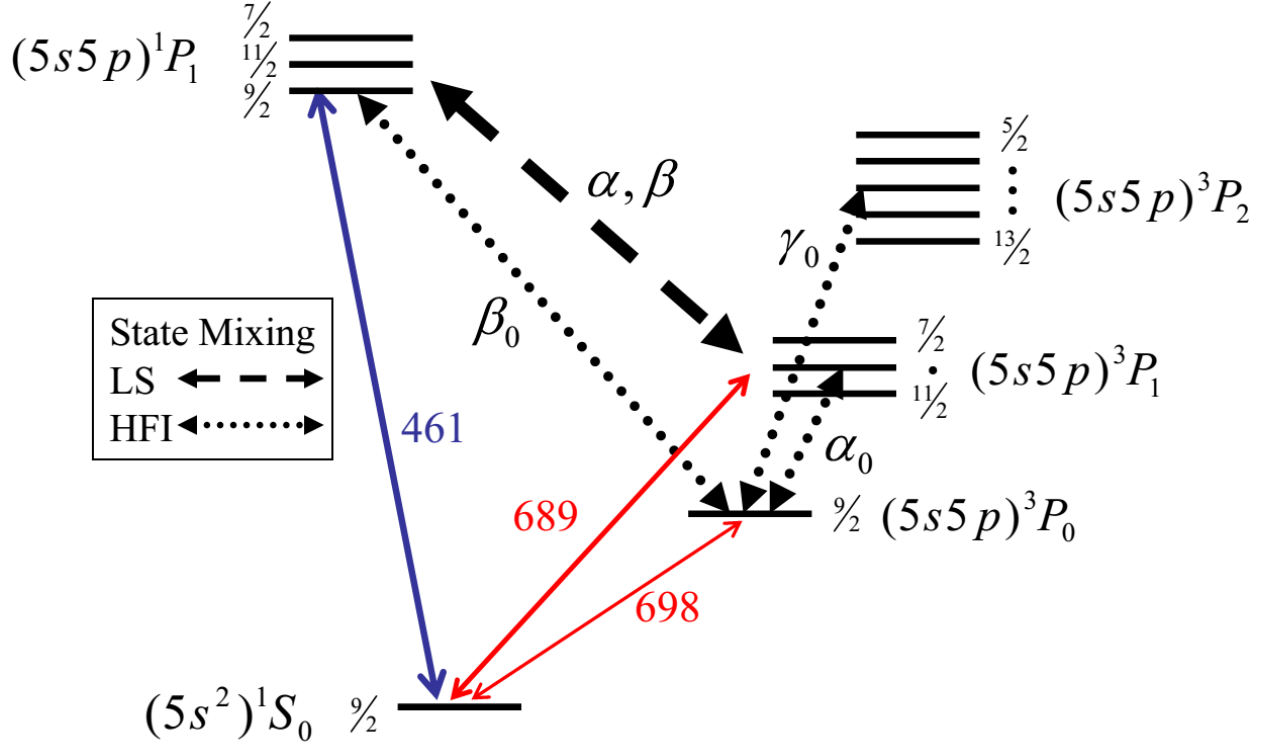


Figure 3. A simplified ^{87}Sr energy level diagram (not to scale) showing the relevant cooling and clock states. States are labeled by their Russel-Saunders term symbol $^{2S+1}L_J$, as described in the text. Energy separation of the levels is reported in the wavelength of the light emitted (nanometers). Hyperfine structure sublevels are denoted by total angular momentum F . The state mixing that arises from spin-orbit coupling (the hyperfine interaction), characterized by mixing coefficients α, β ($\alpha_0, \beta_0, \gamma_0$), is represented by the dashed (dotted) lines. Adapted from [11].

$\Delta J = 1$ which is allowed by the electric dipole selection rules in the LS coupling scheme. The other transitions are not allowed by the electric dipole selection rules: both the second cooling and the clock transitions have $\Delta S = 1$. Furthermore, the clock transition has $J = 0 \rightarrow J = 0$, which isn't allowed in any order transition. Thus we say that the $^1S_0 - ^3P_1$ transition is forbidden and the $^1S_0 - ^3P_0$ transition is doubly forbidden. But these transitions are the cornerstone of the experiment – what is going on here?

The electric dipole selection rules quoted above are only valid in the LS coupling scheme. The spin-orbit interaction term, $\sum_i \zeta(r_i) \hat{l}_i \cdot \hat{s}_i$, does not commute with $\hat{L}_z, \hat{S}_z, \hat{S}^2$ or \hat{L}^2 , but it does commute with \hat{J}_z and \hat{J}^2 . Thus, for an atom with a large spin-orbit interaction, L and S are no longer good quantum numbers and the states $^{2S+1}L_J$ are not eigenfunctions of the Hamiltonian [25]. The

prefactor $\zeta(r_i)$ is proportional to Z^4 , and can be neglected for atoms with small Z . For strontium ($Z = 38$), the spin-orbit interaction is of the same order as the electron-electron Coulomb interaction, and the $^{2S+1}L_J$ states are only approximately eigenfunctions of the Hamiltonian. That is, we will still label the states in the $^{2S+1}L_J$ basis, but this basis is not constructed out of eigenfunctions. As a result, there is some mixing between the states. This is called the intermediate coupling scheme.

The states with maximum or minimum total angular momentum J are unaffected by the spin-orbit mixing, because they are not degenerate in J . The other states are mixed as [24, 26]

$$\begin{aligned} |^3P_0\rangle &= |^3P_0^0\rangle, \\ |^3P_1\rangle &= \alpha|^3P_1^0\rangle + \beta|^1P_1^0\rangle, \\ |^3P_2\rangle &= |^3P_2^0\rangle, \\ |^1P_1\rangle &= -\beta|^3P_1^0\rangle + \alpha|^1P_1^0\rangle, \end{aligned} \quad (2)$$

with the normalization condition $\alpha^2 + \beta^2 = 1$. Here, the superscript (0) indicates a pure state in the LS -coupling scheme. Thus, spin-orbit coupling in strontium makes the second cooling transition an electric dipole transition.

The spin-orbit mixing coefficients α, β can be determined from measured lifetimes and transition frequencies of the 1P_1 and 3P_1 states. For example, consider the electric dipole matrix element between the second cooling and ground states, D_{3P_1} :

$$\begin{aligned} \langle ^1S_0 | \hat{D} | ^3P_1 \rangle &= \langle ^1S_0 | \hat{D} (\alpha|^3P_1^0\rangle + \beta|^1P_1^0\rangle) \\ &= \alpha \langle ^1S_0 | \hat{D} | ^3P_1^0 \rangle + \beta \langle ^1S_0 | \hat{D} | ^1P_1^0 \rangle \\ &= \beta \langle ^1S_0 | \hat{D} | ^1P_1^0 \rangle. \end{aligned} \quad (3)$$

The last equality follows from the dipole selection rules. Using Einstein's relations [27], the lifetime of the state 3P_1 is

$$\tau_{3P_1} = \frac{1}{A_{3P_1}} \propto \frac{1}{\omega_{3P_1}^3 |D_{3P_1}|^2} = \frac{1}{\omega_{3P_1}^3 \beta^2 |\langle ^1S_0 | \hat{D} | ^1P_1^0 \rangle|^2}. \quad (4)$$

Similarly,

$$\langle ^1S_0 | \hat{D} | ^1P_1 \rangle = \alpha \langle ^1S_0 | \hat{D} | ^1P_1^0 \rangle, \quad (5)$$

and

$$\tau_{1P_1} = \frac{1}{A_{1P_1}} \propto \frac{1}{\omega_{1P_1}^3 |D_{1P_1}|^2} = \frac{1}{\omega_{1P_1}^3 \alpha^2 |\langle ^1S_0 | \hat{D} | ^1P_1^0 \rangle|^2}. \quad (6)$$

Combining Eq. (4) & (6) eliminates the unknown matrix element:

$$\frac{\alpha^2}{\beta^2} = \frac{\tau_{3P_1}}{\tau_{1P_1}} \left(\frac{\omega_{3P_1}}{\omega_{1P_1}} \right)^3. \quad (7)$$

Using the measured lifetimes ($\tau_{1P_1} = 5.22(3)$ ns and $\tau_{3P_1} = 21.4(1)$ μ s) and transition frequencies, along with the normalization constraint $\alpha^2 + \beta^2 = 1$, one can calculate the coefficients: $\alpha = 0.9996$ and $\beta = -2.86(3) \times 10^{-2}$ [24].

When considering the hyperfine interaction term for ^{87}Sr , we must include up to electric quadrupole terms since I is so large [25]. The magnetic dipole component is proportional to $\hat{I} \cdot \hat{J}$ and the electric quadrupole term is proportional to terms up to $(\hat{I} \cdot \hat{J})^2$. The situation is analogous to the spin-orbit case in that $F = I + J$ is a good quantum number, but I and J separately are not [11]. Consequently, the hyperfine interaction in ^{87}Sr mixes states that have the same F , i.e. the pure 3P_0 state gets mixed with 3P_1 , 3P_2 and 1P_1 states [24]:

$$|^3P_0\rangle = |^3P_0^0\rangle - \alpha_0 |^3P_1\rangle + \beta_0 |^1P_1\rangle + \gamma_0 |^3P_2^0\rangle. \quad (8)$$

The hyperfine mixing coefficients have approximate values $\alpha_0 \approx 2 \times 10^{-4}$, $\beta_0 \approx -4 \times 10^{-6}$ and $\gamma_0 \approx -1 \times 10^{-6}$ [24]. Combining Eq. (2) & (8) gives the combined effect of spin-orbit and hyperfine mixing on the 3P_0 state in ^{87}Sr [24]

$$|^3P_0\rangle = |^3P_0^0\rangle + (\alpha_0\alpha - \beta_0\beta) |^3P_1^0\rangle + (\alpha_0\beta - \beta_0\alpha) |^1P_1^0\rangle + \gamma_0 |^3P_2^0\rangle. \quad (9)$$

Thus the finite lifetime of the clock state is a consequence of the combination of the spin-orbit and hyperfine interactions. The spin-orbit mixing coefficient is two orders of magnitude larger than its hyperfine counterparts, indicating the relative strength of the two interactions.

The hyperfine mixing leads to other unexpected effects. One that is crucial for the clock experiment is the *differential Landé g-factor* between the ground state and the clock state. Without hyperfine mixing, the 3P_0 g-factor would be the same as the 1P_0 g-factor; thus the first order Zeeman shift between the two states would be zero. The hyperfine mixing modifies the 3P_0 state according to Eq. (9), and the differential Zeeman shift between the two states is nonzero. To see how this comes about, we can write down the Hamiltonian for the first order Zeeman effect with a weak magnetic field B along the z axis:

$$\hat{H}_{\text{Zeeman}} = (g_s \hat{S}_z + g_l \hat{L}_z - g_I \hat{I}_z) \mu_B B, \quad (10)$$

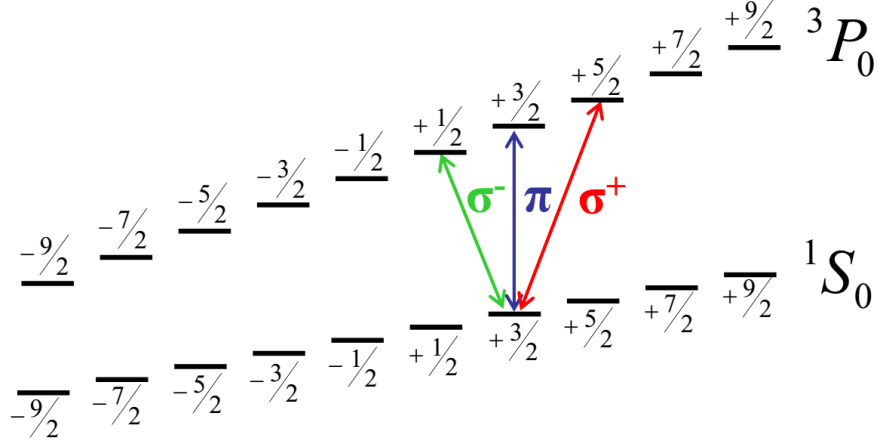


Figure 4. The clock transition of ^{87}Sr in a small magnetic field. There are $2F + 1 = 10$ sublevels for each state; numbers indicate the value of m_F . The differential Landé g factor manifests itself as a linear Zeeman shift for the $^1S_0 - ^3P_0$ transition. Arrows indicate the σ^- , π and σ^+ transitions, where m_F changes by -1 , 0 , and $+1$, respectively. Adapted from [28].

where $g_s \simeq 2$, $g_l = 1$, $g_I \simeq -1 \times 10^{-4}$ are the spin, orbital and nuclear g -factors, respectively. It can be shown [24] that the differential g -factor between the two states is

$$\delta g = -(\alpha_0 \alpha - \beta_0 \beta) \sqrt{\frac{8}{3I(I+1)}} \simeq -6 \times 10^{-5}, \quad (11)$$

and the differential frequency shift is given by

$$\Delta_B^{(1)} = -\delta g m_F \frac{\mu_B}{h} B \simeq m_F \times 110 \frac{\text{Hz}}{\text{G}}. \quad (12)$$

Both the ground and clock states have $2F + 1 = 10$ different m_F sublevels (see Fig. 4). The differential Zeeman shift can be eliminated by pumping the ground state to two opposite m_F numbers, say $\pm 9/2$, and averaging their transition frequencies (see Fig 8a). Unless the ground state is prepared to a single m_F number, the clock frequency will broaden in the presence of a magnetic field. Conversely, one can use this effect to stabilize the magnetic field inside the clock chamber (see Fig. 8b). Both of these techniques are used in the JILA clock [1].

Blackbody Radiation (BBR) Frequency Shift

The atoms in the optical clock are held at μK temperatures in an optical lattice. However, the optical lattice is inside a room-temperature vacuum chamber. The blackbody radiation emitted by

the surrounding environment perturbs the electronic states of the atoms, and the resulting fractional frequency shift ($\approx 10^{-15}$) is the dominant systematic error of the ^{87}Sr clock [1]. Understanding and correcting this frequency shift is essential for accuracy at the 10^{-18} level. The basic theory behind the blackbody radiation (BBR) shift will be discussed in this section.

The physical mechanism behind the BBR shift is the Stark shift, which can be calculated using perturbation theory [29–33]. Consider the effect of a monochromatic electric field $\vec{E}(\omega)$ on a state $|a\rangle$. We will only consider the electric dipole contribution of the radiation (this approximation will be justified below). The first order energy shift is zero, and the second order energy shift is [25]

$$\delta E_a = \sum_{b \neq a} \frac{|\langle b | \hat{H}_I | a \rangle|^2}{\mathcal{E}_a - \mathcal{E}_b}. \quad (13)$$

Here, the perturbation is $\hat{H}_I = -\hat{\vec{\mu}} \cdot \vec{E} = e\hat{\vec{r}} \cdot \vec{E}(\omega)$. When calculating the energy denominator, we consider the “atom plus field” system [34]. In state $|a\rangle$, the atom has energy E_a and the field (containing n photons) has energy $n\hbar\omega$, so $\mathcal{E}_a = E_a + n\hbar\omega$. If the atom is excited to state $|b\rangle$ by absorbing a photon, it has internal energy E_b and the field has energy $(n-1)\hbar\omega$, so $\mathcal{E}_b = E_b + (n-1)\hbar\omega$. In this case, the energy difference is $\mathcal{E}_a - \mathcal{E}_b = E_a - E_b + \hbar\omega = \hbar(\omega_{ab} + \omega)$. Note that because these are bound states, $\hbar\omega_{ab} = E_a - E_b$ is negative for states $|b\rangle$ lying above $|a\rangle$ and positive for states $|b\rangle$ lying below $|a\rangle$. If the atom is relaxed to state $|b\rangle$ by emitting a photon, then $\mathcal{E}_b = E_b + (n+1)\hbar\omega$ and $\mathcal{E}_a - \mathcal{E}_b = \hbar(\omega_{ab} - \omega)$. We allow for both possibilities [11, 31]:

$$\delta E_a(\omega) = \frac{1}{4} \sum_{b \neq a} \frac{|\langle a | e\hat{\vec{r}} \cdot \vec{E}(\omega) | b \rangle|^2}{\hbar} \left(\frac{1}{\omega_{ab} - \omega} + \frac{1}{\omega_{ab} + \omega} \right). \quad (14)$$

The factor of $1/4$ comes from the complex representation of $\vec{E}(\omega)$. For future reference, we define the *dynamic dipole polarizability* of state $|a\rangle$ as

$$\alpha_a(\omega) = \frac{e^2}{\hbar} \sum_{b \neq a} |\langle a | \hat{x} | b \rangle|^2 \left(\frac{1}{\omega_{ab} - \omega} + \frac{1}{\omega_{ab} + \omega} \right) = 2\pi\epsilon_0 c^3 \sum_{b \neq a} \frac{2J_b + 1}{2J_a + 1} \frac{A_{ba}}{\omega_{ab}^2 (\omega_{ab}^2 - \omega^2)}, \quad (15)$$

where A_{ba} is the Einstein coefficient for the two states $|a\rangle$ and $|b\rangle$, and J_a is the total angular momentum of state $|a\rangle$ [7]. In this notation, the ac-Stark shift can be written as

$$\delta E_a(\omega) = \frac{1}{4} \alpha_a(\omega) E(\omega)^2. \quad (16)$$

This form will be useful in a later discussion. Going back to Eq. (14), we can relate the electric field amplitude to blackbody temperature T using the Planck formula for BBR spectral energy density $u_\omega(T)$ [30]:

$$u_\omega(T) = \frac{\hbar}{\pi^2 c^3} \frac{\omega^3}{e^{\hbar\omega/k_B T} - 1} = \frac{\epsilon_0 E(\omega)^2}{2} = \frac{3\epsilon_0 E_x(\omega)^2}{2}. \quad (17)$$

The last equality follows from the isotropic nature of the BBR field. Now, we integrate over the entire spectrum to get the total electric dipole shift of state $|a\rangle$ in the presence of a radiating black body:

$$\Delta E_a = \frac{3e^2}{4\pi^2 c^3 \epsilon_0} \sum_{b \neq a} |\langle a | \hat{x} | b \rangle|^2 \mathcal{P} \int_0^\infty d\omega \frac{\omega^3}{e^{\hbar\omega/k_B T} - 1} \left(\frac{1}{\omega_{ab} - \omega} + \frac{1}{\omega_{ab} + \omega} \right). \quad (18)$$

The symbol \mathcal{P} denotes the Cauchy principal value. We can extract the temperature dependence of the BBR shift by making the substitutions $x = \hbar\omega/k_B T$ and $y = \hbar\omega_{ab}/k_B T$:

$$\Delta E_a = \frac{3e^2}{4\pi^2 c^3 \epsilon_0} \left(\frac{k_B T}{\hbar} \right)^3 \sum_{b \neq a} |\langle a | \hat{x} | b \rangle|^2 \mathcal{P} \int_0^\infty dx \frac{x^3}{e^x - 1} \left(\frac{1}{y - x} + \frac{1}{y + x} \right). \quad (19)$$

The sensitivity of the atom to the BBR spectrum is contained within the dimensionless integral on the right side of the equation. This integral, which we identify as $F(y)$, is odd and only depends the ratio of the transition energy to the thermal energy. Numerically evaluating the integral reveals that it vanishes at the origin and at $y = 2.616$; it is negative for $0 \leq y \leq 2.616$ and positive for $y > 2.616$. Thus, nearby states ($|y| < 2.616$) attract the shifted state while distant states repel the shifted state [31]. In the region $|y| > 10$, where the transition energy is much larger than the thermal energy, we can approximate $F(y)$ as [30]

$$F(y) = \frac{2}{3\pi} \mathcal{P} \int_0^\infty dx \frac{x^3}{e^x - 1} \left(\frac{1}{y - x} + \frac{1}{y + x} \right) \approx \frac{4\pi^3}{45y} + \frac{32\pi^5}{189y^3} + \frac{32\pi^7}{45y^5} + \frac{512\pi^9}{99y^7}. \quad (20)$$

Recalling the definitions of x and y , we see that the first term in the expansion of Eq. (19) is proportional to T^4 and the static dipole polarizability $\alpha_a(\omega = 0)$; the second term is proportional to T^6 , and so on. We are interested in the frequency shift between the ground state 1S_0 and the clock state 3P_0 , so we calculate the shift for both levels and take the difference. Lumping all terms higher than T^4 into one term, the BBR frequency shift can be cast in the form [7]

$$\Delta \nu^{BBR} = -\frac{1}{2h} \Delta \alpha \langle E^2 \rangle_T + \Delta \nu^{dyn} \left[T^6 + O(T^8) \right], \quad (21)$$

where $\langle E^2 \rangle_T = \int_0^\infty E(\omega)^2 d\omega = (8.319 \text{ V/cm})^2 \times (T/300 \text{ K})^4$ and the coefficient $\Delta \alpha$ is the *differential static polarizability* between the clock state and the ground state. The first term in Eq. (21) is called the *static BBR frequency shift* and the second is the *dynamic BBR frequency shift* [1]. The coefficients can be measured experimentally or calculated from the matrix elements in Eq. (19).

Physically, we can interpret this result as follows. The T^4 term represents the second order Stark shift due to a static field, with a magnitude equal to the *rms* average of the electric field of

the BBR spectrum; the higher order terms are corrections to this approximation by including the effects of small dynamical fluctuations from the average. We may have been able to guess this behavior, since at 300 K most of the blackbody spectrum is at frequencies much lower than the relevant atomic transitions [7].

Before moving on, let's discuss the assumptions that have been made in deriving Eq. (21). First, we have only considered electric dipole ($E1$) contributions to the Stark shift. A full treatment would require multipole expansion of the electromagnetic vector potential. It can be shown that the magnetic dipole ($M1$) term is a factor of $\sim 10^{-4}$ weaker than the $E1$ term, and the electric quadrupole ($E2$) term is a factor of $\sim 10^{-10}$ weaker than the $E1$ term [30]. While the $M1$ term becomes important below the 10^{-18} accuracy level, the error introduced by its omission is less than that introduced by the current uncertainty of $\Delta\alpha$ [32].

We have also assumed that only the transitions with large $|y|$ meaningfully contribute to the BBR shift. Even though there are states close to the clock state 3P_0 with small $|y|$, they are either $M1$ or $E2$ transitions. $F(y)$ can be numerically evaluated for these transitions, and it is found that it is of the same order of magnitude for typical $E1$ transitions. This is a consequence of the broadness of the BBR spectrum. Thus, the effects of these transitions will be suppressed by the very small factors discussed above and can be ignored [29, 30]. In strontium, the dominant contribution of the BBR shift to the comes from the $5s5p\ ^3P_0 - 5s4d\ ^3D_1$ ($E1$) transition, since this transition has a very long wavelength ($2.6\ \mu\text{m}$) [7]. As $y \simeq 18$ and $F(y) \simeq 0.15$ for this transition, the net effect is a repulsion of the 3P_0 from the higher-lying 3D_1 state.

Determining the BBR Coefficients

In 2012, Middelmann *et al.* [7] measured the differential static polarizability in Eq. (21) using a strontium lattice clock. They obtained a value of $\Delta\alpha = 4.07873(11) \times 10^{-39}\ \text{C m}^2/\text{V}$. The value in the parenthesis constitutes a fractional uncertainty of $\approx 2 \times 10^{-5}$. The details of their experiment will be described in this section.

The concept of the experiment was simple: measure the frequency of the $^3P_0 - ^1S_0$ transition as a function of external electric field, which was introduced by a precision capacitor (see Fig. 5a). The capacitor was constructed of low thermal expansion Zerodur glass to prevent a temperature-dependent capacitance. The $28 \times 100\ \text{mm}^2$ plates were coated with 5 nm of aluminum and 20 nm of gold, then separated by two optically contacted 5 mm tall Zerodur blocks. The plates

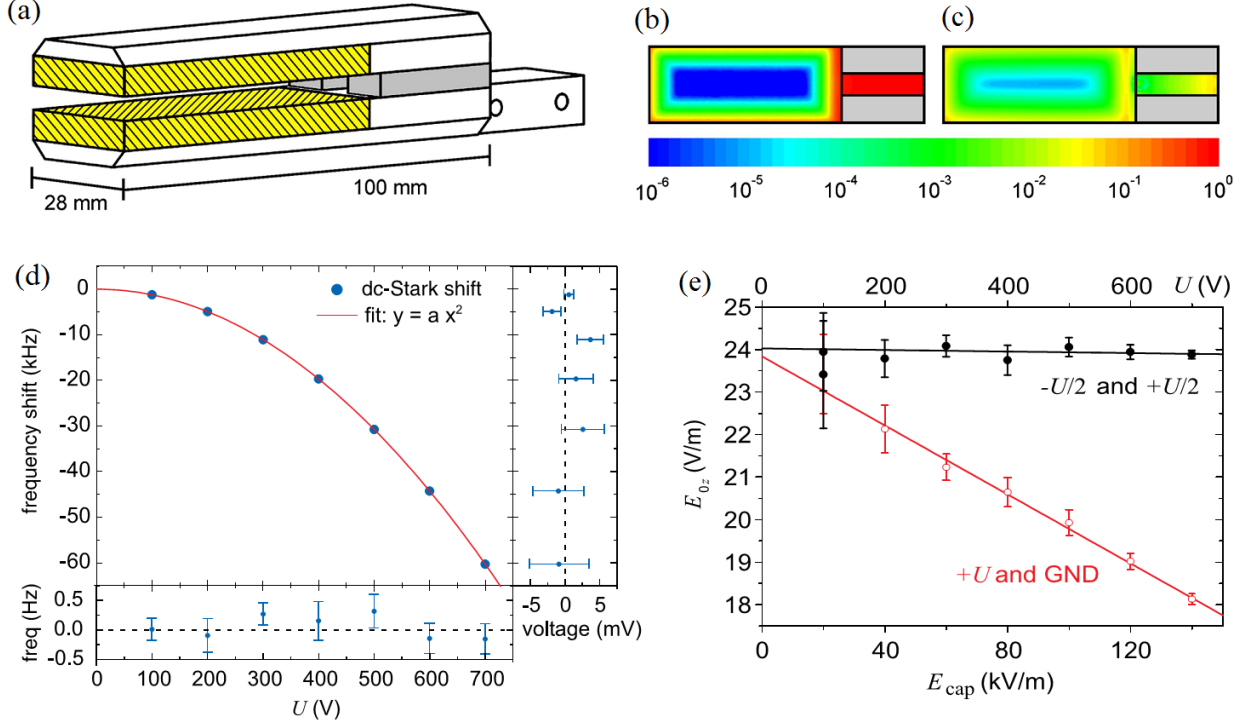


Figure 5. The precision capacitor and measured differential dc-Stark shift. (a) A sketch of the capacitor. The hatched areas depict the gold plated electrodes. (b) Deviation of the electric field at the $z = 0$ plane from an infinite parallel plate capacitor when voltages $\pm U/2$ are applied. (c) z -component of the stray field \vec{E}_0 leaking into the $z = 1$ mm plane when both electrodes are at potential U/d . (d) Measured frequency shift from the capacitor and a fitted parabola with the residuals of the fit. The frequency shift due to the capacitor was determined by Eq. (22). (e) The z -component of \vec{E}_0 , as determined from Eq. (24), plotted as a function of applied voltage U . The simulation results in (b) and (c) are in units of U/d . Adapted from [7].

were found to be non-parallel by an angle of about $5 \mu\text{rad}$, corresponding to a plate separation distance correction of $153(28)$ nm. Including these corrections, the total separation of the plates was determined by interferometry to be $5,001,644 \pm 39.5$ nm. Simulations of the capacitor (Fig. 5b) indicate that the electric field at the center of the capacitor can be determined by $E_{\text{cap}} = U/d$ with an error of about 10^{-6} .

The capacitor was installed inside their existing strontium clock such that the optical lattice could be translated from its normal position to between the capacitor's plates during operation. When a voltage was applied across the plates, the atoms felt an electric field \vec{E}_{cap} from the capacitor, plus a small stray field \vec{E}_0 . Thus, the measured transition frequency was dc-Stark shifted by an amount proportional to $(\vec{E}_{\text{cap}} + \vec{E}_0)^2$. To extract the dc-Stark shift due to \vec{E}_{cap} alone, they

measured three frequency offsets ν_i ($i = \uparrow, \downarrow, 0$) for each voltage U ; each ν_i corresponded to a field configuration $\vec{E}_{cap} = (\vec{E}_{cap}, -\vec{E}_{cap}, 0)$. Assuming the stray field was slowly changing, and ignoring the contribution of the small term E_0^2 , the dc-Stark shift due to the capacitor is

$$\nu_{dc} = \frac{(\nu_{\uparrow} + \nu_{\downarrow})}{2} - \nu_0. \quad (22)$$

Several parabolas were measured (see Fig. 5d), and $\Delta\alpha$ was determined for each voltage U

$$\nu_{dc} = -\frac{\Delta\alpha}{2hd^2}U^2, \quad (23)$$

where d is the capacitor plate separation and h is Planck's constant, as in Eq. (21). The effects of hyperpolarizability (i.e., $\Delta\alpha$ scaling with E^2) were investigated by fitting a parabola of the type $\Delta\alpha(E) = a + bE^2$. The difference between the fitted coefficient a and the weighted average of $\Delta\alpha$ was taken as the fractional uncertainty contribution for the hyperpolarizability, which was 12×10^{-6} .

Understanding the origin of the stray field is important, since it undermines the validity of Fig. 5d. The z -component of the stray field can be experimentally determined from

$$\nu_{\uparrow} - \nu_{\downarrow} \propto \vec{E}_{cap} \cdot \vec{E}_0 = E_{cap}E_{0z}. \quad (24)$$

The z -component of the stray field is plotted in Fig. 5e as a function of the applied voltage, using two different configurations. The first configuration (black curve) was with the plates at potentials $\pm U/2$; the second configuration (red curve) was with both plates at $+U/2$. The origin of the stray field \vec{E}_0 was twofold. Imperfections in the gold-coating process lead to the so-called patch effect, where spatial variations of the work function produce a voltage-independent electric field (black curve). Second, the atoms will experience a voltage-dependent electric field if they were not exactly on the symmetry axis ($z = 0$ plane) of the capacitor (red curve). A second simulation of the capacitor (see Fig. 5c) indicates that an offset of 1 mm from the symmetry plane of the capacitor can explain voltage dependence of the stray field.

With an improved value of $\Delta\alpha$ in hand, Middelmann *et al.* were able to calculate the dynamic coefficient $\Delta\nu^{dyn}$ in Eq. (21). Using literature values of various experimental parameters (magic wavelength [20], atomic lifetimes, ac-Stark shifts of the clock laser field, etc.) they back-calculated the Einstein coefficients A_{ab} for each transition. They used a least squares fit of the resulting A_{ab} 's to combine the data from multiple sources. Then, they wrote ac-Stark shift in the form of Eq. (16) and $\alpha_a(\omega)$ in terms of the Einstein coefficients A_{ab} , as in the far right side of Eq. (15). Finally, they

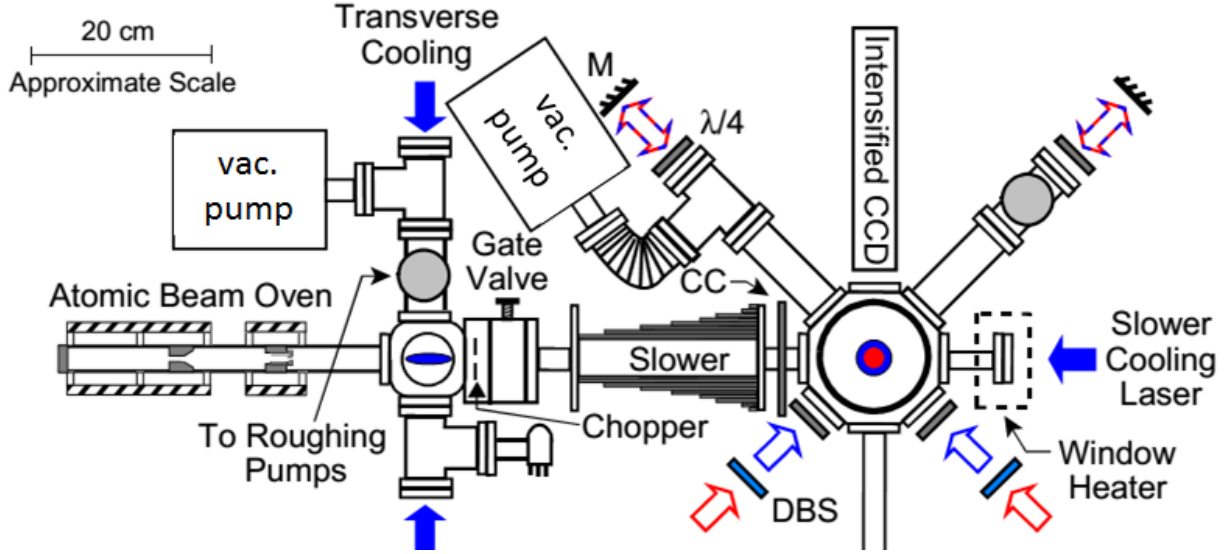


Figure 6. Schematic of the experimental apparatus for cooling and trapping strontium. Arrows and colored circles indicate the laser pathways. The right window must be heated to prevent Sr buildup; this is a potential source of BBR shifts. See text for details. DBS: dichroic beam splitter, M: mirror, CC: compensation coil. Adapted from [13].

integrated this expression over the Planck distribution to obtain the coefficient $\Delta v^{dyn} = -147.6(23)$ mHz.

Putting it all together, the BBR frequency shift can be written as

$$\Delta v^{BBR}(T) = -2.13023(6) \text{ Hz} \left(\frac{T}{T_0} \right)^4 - 147.6(23) \text{ mHz} \left[\left(\frac{T}{T_0} \right)^6 + O\left(\frac{T}{T_0} \right)^8 \right], \quad (25)$$

with $T_0 = 300$ K.

Case Study: The ^{87}Sr Optical Clock at JILA

The operation of an optical clock relies upon a myriad of established techniques and technologies. The first step is obtaining a supply of cold ^{87}Sr atoms to reduce Doppler broadening; see Fig. 6 and Tab. I for experimental details and Fig. 3 for the relevant transitions. First, elemental strontium is heated under vacuum in an effusion oven. The resulting gas is collimated by passing through a couple of ~ 1 mm diameter nozzles and a two-dimensional transverse cooling region (optical molasses) that uses 10-20 mW of light. The collimated beam enters a 20 cm long constant deceleration σ^- Zeeman slower with a peak magnetic field of 600 G, where the atoms are

Cooling Step	Transition	Detuning (MHz)	Initial speed (temp.)	Final speed (temp.)
Transverse Cooling	$^1S_0 - ^1P_1$	-10	N/A	N/A
Zeeman Slower		-1,030	500 m/s (1,000 K)	30 m/s (3 K)
Broad MOT		-40	30 m/s (3 K)	50 cm/s (2.5 mK)
Intercombination MOT	$^1S_0 - ^3P_1$	a few	50 cm/s (2.5 mK)	3 cm/s (3 μ K)

Table I. Laser cooling summary [11, 13]. Detuning the laser from resonance compensates for Doppler and Zeeman shifts.

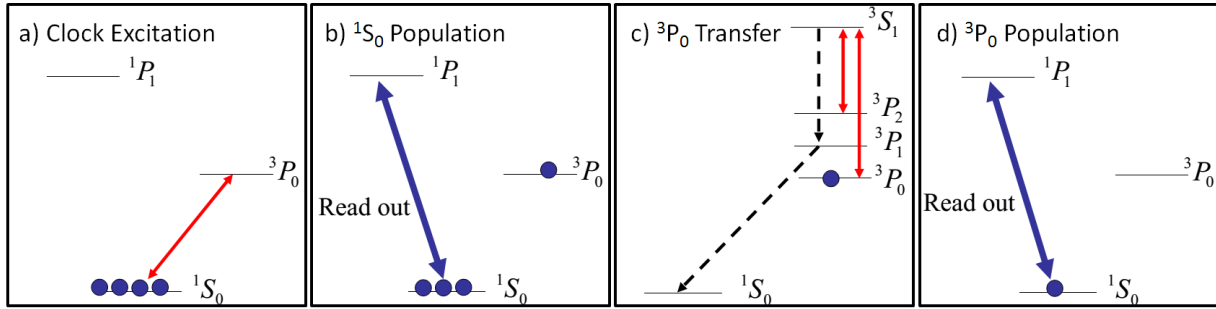


Figure 7. Clock interrogation scheme. The blue dots are a cartoon representation of the population of electronic states. Adapted from [11].

slowed using 60 mW of light. Stray fields from the Zeeman slower are minimized by three sets of Helmholtz pairs. After exiting the Zeeman slower, the atoms are further cooled by a series of magneto-optical traps (MOTs). The first MOT utilizes the 461 nm $^1S_0 - ^1P_1$ broad (30 MHz) transition to cool the atoms using 30 mW of light in each beam. The second MOT uses the 689 nm $^1S_0 - ^3P_1$ narrow (7.5 kHz) intercombination transition [16]. The second MOT uses dual-frequency narrow line cooling, with one frequency red-detuned from the $^1S_0(F = 9/2) - ^3P_1(F = 11/2)$ transition and the other red-detuned from $^1S_0(F = 9/2) - ^3P_1(F = 9/2)$. Both lasers are frequency modulated to broaden their linewidths to a few megahertz, comparable to the Doppler-broadened profile of the atoms from the first MOT [35].

The 461 nm (blue) light is produced [11] by frequency doubling the output of a 922 nm diode laser. The frequency of the blue light is stabilized to a ^{88}Sr saturated absorption spectrometer. Acoustic-optic modulators (AOMs) are used to detune the light before being used for the slower and MOTs. The 689 nm light source is another diode laser stabilized to a high finesse cavity ($F \sim 3,000$) using an electro-optical modulator (EOM) to modulate the laser frequency for the

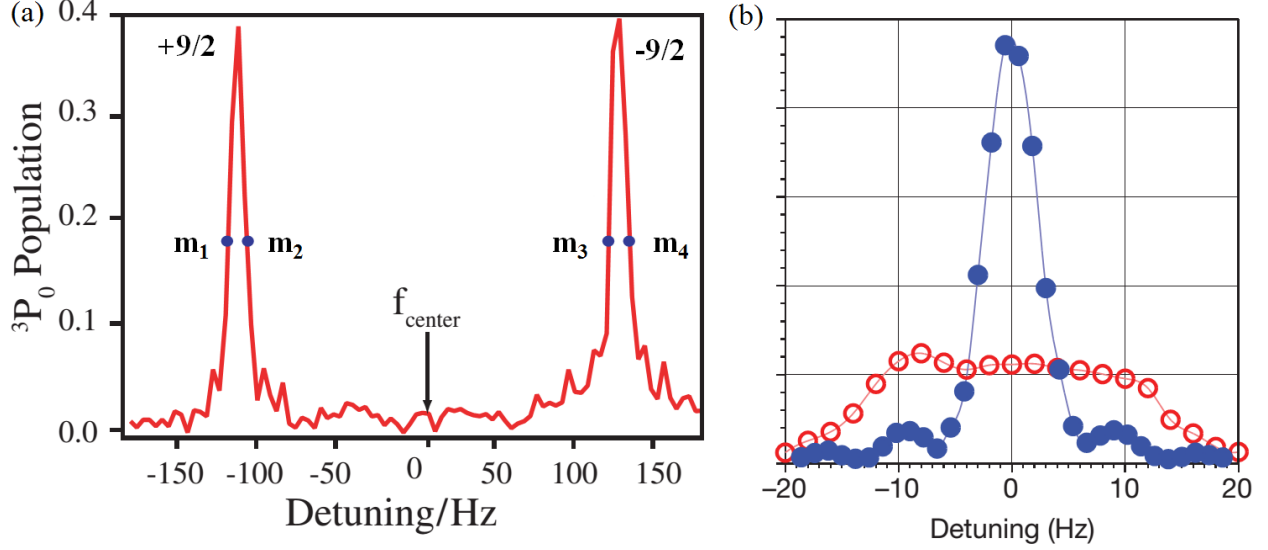


Figure 8. Clock spectroscopy data in a magnetic field. (a) Composite data from many clock interrogations showing two peaks corresponding to a spin polarized atomic cloud with $m_F = \pm 9/2$. Blue dots indicate FWHM points used to find the center frequency of each peak. Based on the separation of the two peaks, the magnetic field is about 20 μT . The average of the two frequencies eliminates the first order Zeeman dependence. Adapted from [35]. (b) Using the Rabi lineshape to zero the magnetic field. Atoms were *not* spin polarized, thus all m_F states were populated. Open red circles correspond to an unstabilized magnetic field (about 3 μT); blue points show an improved lineshape with a stabilized field ($< 0.5 \mu\text{T}$). Adapted from [1].

Pound-Drever-Hall (PDH) technique [36].

Approximately 10^3 atoms [16] are then loaded into a 1D optical lattice [34] near the magic wavelength $\lambda_m = 813.428 \text{ nm}$. The lattice is operated in the Lamb-Dick regime by making the optical lattice trap depths between $40E_r$ and $300E_r$, where $E_r = h\nu_r$ is the photon recoil energy [1]. In preparation for the clock spectroscopy the atoms are optically pumped to the stretched $|F = 9/2, m_F = \pm 9/2\rangle$ states via the $^1S_0(F = 9/2) - ^3P_1(F = 7/2)$ transition [11, 35]. The system is now ready to be interrogated using Rabi spectroscopy.

The Rabi spectroscopy proceeds as follows [11, 35, 37]. A thermal-noise limited 698 nm diode laser with short-term stability of 1×10^{-16} is used to interrogate the 698 nm $^1S_0 - ^3P_0$ transition as depicted in Fig. 7. The light is produced by a 698 nm grating-stabilized diode laser that is locked to a high-finesse ($F \sim 200,000$) ultrastable, ultra-low-expansion (ULE) cavity [1, 35, 37, 38] using the PDH technique. First, a 160 ms Rabi pulse is used to induce a π -transition ($\Delta m_F = 0$, see Fig.

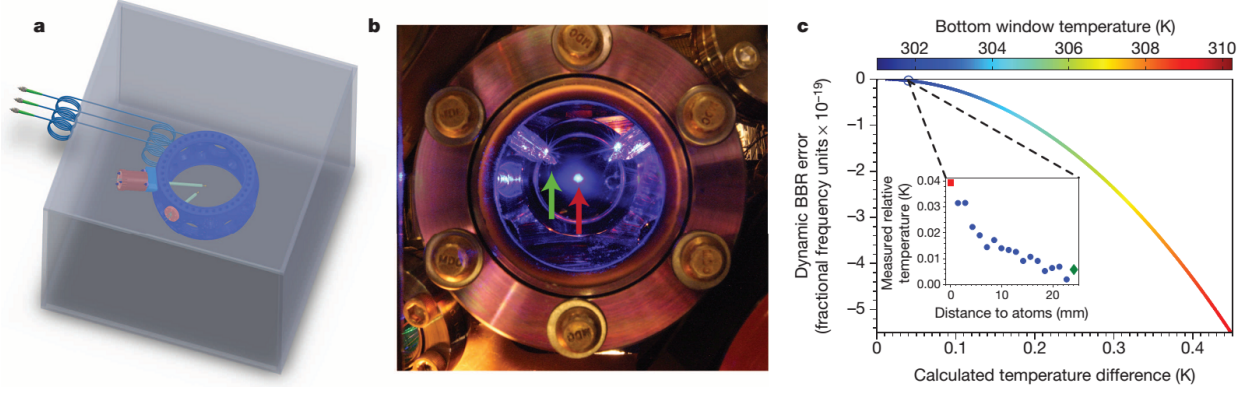


Figure 9. Black-body radiation in the SrII optical clock. (a) A 3D rendering of BBR shielding box showing the fiber optics and temperature sensors. (b) A photograph of the clock during operation. The atoms can be seen fluorescing (red arrow); the temperature sensor is retracted (green arrow). (c) Results of a ray-tracing simulation showing the error introduced by applying the thermometer readout to calculate the dynamic BBR shift. To give a sense of the temperature gradients inside the chamber, the inset shows the measured temperatures as a function of the thermometer - atom distance. The red square is the atomic position; the green diamond is the retracted position. Adapted from [1].

4) by exciting a fraction of the ground state into the clock state (Fig. 7a). The 3P_0 clock state is stable for ~ 150 seconds, and the remaining ground state population is detected using fluorescence between the $461 \text{ nm } ^1S_0 - ^1P_1$ transition (Fig. 7b). In the process of measuring the ground state population, these atoms are heated out of the trap [35]. Next, the atoms in the clock state are brought back to the ground state using a series of intermediate transitions (Fig. 7c). This requires repumping lasers at 679 nm (for $^3P_0 \rightarrow ^3S_1$) and 707 nm (for $^3P_2 \rightarrow ^3S_1$), since 3S_1 can decay into any of the states in the 3P_J manifold. Once the $^3P_0 \rightarrow ^1S_0$ transition is complete, the ground state population is measured again by $461 \text{ nm } ^1S_0 - ^1P_1$ fluorescence (Fig. 7d). The second population measurement is normalized to the first, yielding the excitation fraction from the initial $^1S_0 \rightarrow ^3P_0$ transition.

The process of cooling, trapping, pumping and interrogating the atoms takes about 1.3 seconds, and will obtain one data point on the plot shown in Fig. 8. In practice only the frequencies near the peaks are investigated. Measuring the transition frequency of a given state is an iterative process. For example, to calculate the transition frequency for $m_F = -9/2$, data is taken at the approximate full width at half maximum (FWHM) points, labeled m_3 and m_4 in Fig. 8a. If the population at these points is equal, then the frequency corresponding to their midpoint is the transition frequency.

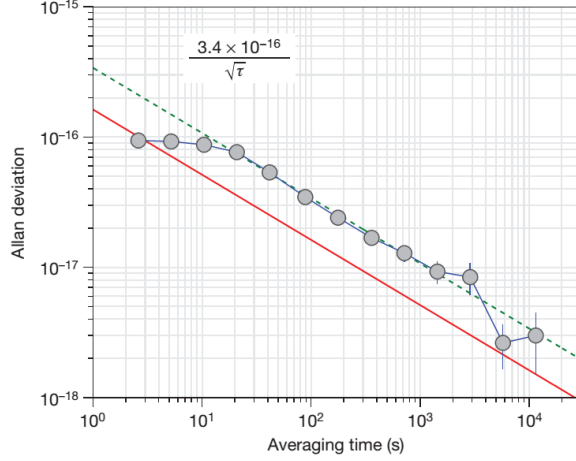


Figure 10. Allan deviation of the SrI and SrII comparison plotted as a function of averaging time τ . The Allan deviation has been divided by $\sqrt{2}$ to reflect the performance of a single clock. The solid red line is the calculated quantum projection noise for this configuration. The green dashed line is a fit to the data, showing an Allan deviation of $3.4 \times 10^{-16}/\sqrt{\tau}$. Adapted from [1].

Otherwise, a PID algorithm is implemented to efficiently take more data points until the transition frequency is known [13]. This process is repeated for both $m_F = \pm 9/2$ states. The average of the two transition frequencies is used to eliminate the first-order Zeeman effect [35, 37].

Ye's group operates two separate ^{87}Sr clocks (named SrI and SrII) simultaneously in this fashion [1, 16]. As its name suggests, SrII is more advanced than SrI. SrII's optical trap volume is about 100 times larger than that of SrI, which results in a lower atomic density [16] and smaller density-related frequency shifts [39] during clock operation. The uncertainty of the density shift of SrII is 1×10^{-18} [1]. To reduce the influence of exterior heat sources, the entire clock apparatus of SrII is enclosed in a shielding box (see Fig. 9a). Fiber optics are used to deliver the cooling, trapping and clock spectroscopy lasers to the atoms to minimize the radiation inside the cavity. Two silicon diode thermometers are used to provide real-time temperature data of the clock. The first thermometer is fixed 1 inch away from the lattice; the second one is attached to a translating stage to map out temperature gradients after the box has reached thermal equilibrium.

The thermometers are capable of measuring the thermal distribution at the position of the atoms with an uncertainty of 26.7 mK. This temperature reading can be used to calculate the static BBR shift in Eq. (25). Some care must be taken in calculating the dynamic BBR shift, however. The reported temperature corresponds to the integrated radiation spectrum, but it doesn't contain any information about the shape of the spectrum. Looking back at the derivation of Eq. (25), we

can see that the dynamic BBR term depends on the frequency-weighted spectrum of the radiation experienced by the atoms. This wouldn't be a problem if the radiation in the chamber was due to an ideal black body source. However, a temperature gradient in the chamber will result in a spectrum that is different than the one described by Eq. (17), thus introducing error into the calculated dynamic BBR term.

This error was estimated by making a ray-tracing model of the SrII clock chamber. All components of the chamber were modeled as having the same temperature ($T = 301$ K), with the exception of the bottom window (shown in Fig. 9b). As the bottom window temperature is varied, the dynamic BBR shift is calculated in two ways: via a simulated thermometer reading (which mimics the actual experiment) and via the frequency-weighted spectrum of the radiation (which is the correct way to calculate the BBR shift). The error of using the thermometer temperature is plotted in Fig. 9c, showing that a bottom window temperature of 310 K results in a dynamic BBR error of -5×10^{-19} .

The magnetic field in each clock was zeroed by using the atoms as a magnetometer. The field strength was measured by performing Rabi spectroscopy on unpolarized atoms as in Fig. 8b. As discussed after Eq. (12), the lineshape of unpolarized atoms will broaden in the presence of a magnetic field. Owing to its larger interaction volume, it is harder to control the magnetic fields in SrII. SrII uses an iterative algorithm, where three pairs of magnetic field compensation coils adjust the field to minimize the width of the lineshape. This algorithm is run once every two minutes, keeping the magnetic field below $0.3 \mu\text{T}$.

To evaluate stability, the two clocks are compared against each other, as shown in Fig. 10. The major contributions to the instability are from the laser and the quantum projection noise. The combined stability is reported as $3.4 \times 10^{-16}/\sqrt{\tau}$, meaning that the clocks can reach the level of 3×10^{-18} in about 10,000 seconds. The statistical uncertainty matches the total systematic uncertainty within 3,000 seconds.

Conclusion

Three main techniques and technologies are responsible for the increased performance of optical atomic clocks since the turn of the century: optical cooling and trapping of atoms, femtosecond frequency combs and ultrastable lasers [4]. Beyond these technical achievements, understanding the systematic effects in optical lattice clocks is essential for improving their accuracy. In the case

study discussed here, characterizing the BBR shift was responsible for a factor of 22 improvement in clock uncertainty (i.e., accuracy) compared to previous optical lattice clocks [1]. Additional improvements in laser stability will lead to a further reduction in clock instability, which is rapidly approaching the quantum limit [16]. It is only a matter of time before the SI second is redefined to correspond to the transition used in ^{87}Sr optical lattice clocks [19].

* smith.8391@osu.edu

- [1] B. J. Bloom, T. L. Nicholson, J. R. Williams, S. L. Campbell, M. Bishof, X. Zhang, W. Zhang, S. L. Bromley, and J. Ye, *Nature* **506**, 71 (2014).
- [2] T. Rosenband, D. B. Hume, P. O. Schmidt, C. W. Chou, A. Brusch, L. Lorini, W. H. Oskay, R. E. Drullinger, T. M. Fortier, J. E. Stalnaker, S. A. Diddams, W. C. Swann, N. R. Newbury, W. M. Itano, D. J. Wineland, and J. C. Bergquist, *Science* **319**, 1808 (2008).
- [3] A. D. Ludlow, S. Blatt, T. Zelevinsky, G. K. Campbell, M. J. Martin, J. W. Thomsen, M. M. Boyd, and J. Ye, *The European Physical Journal Special Topics* **163**, 9 (2008).
- [4] S. A. Diddams, T. Udem, J. C. Bergquist, E. A. Curtis, R. E. Drullinger, L. Hollberg, W. M. Itano, W. D. Lee, C. W. Oates, K. R. Vogel, and D. J. Wineland, *Science* **293**, 825 (2001).
- [5] A. G. Smart, *Physics Today* **67**, 12 (2014).
- [6] S. A. Diddams, J. Ye, and L. Hollberg, “Femtosecond lasers for optical clocks and low noise frequency synthesis,” in *Femtosecond Optical Frequency Comb Technology: Principle, Operation and Applications*, edited by J. Ye and S. T. Cundiff (2005).
- [7] T. Middelmann, S. Falke, C. Lisdat, and U. Sterr, *Phys. Rev. Lett.* **109**, 263004 (2012).
- [8] S. R. Jefferts, T. P. Heavner, T. E. Parker, and J. H. Shirley, *Acta Physica Polonica A* **112**, 759 (2007).
- [9] S. A. Diddams, D. J. Jones, J. Ye, S. T. Cundiff, J. L. Hall, J. K. Ranka, R. S. Windeler, R. Holzwarth, T. Udem, and T. W. Hänsch, *Phys. Rev. Lett.* **84**, 5102 (2000).
- [10] J. Ye and S. T. Cundiff, “Introduction,” in *Femtosecond Optical Frequency Comb Technology: Principle, Operation and Applications*, edited by J. Ye and S. T. Cundiff (2005).
- [11] M. M. Boyd, *High Precision Spectroscopy of Strontium in an Optical Lattice: Towards a New Standard for Frequency and Time*, Ph.D. thesis, University of Colorado (2007).
- [12] N. Hinkley, J. A. Sherman, N. B. Phillips, M. Schioppo, N. D. Lemke, K. Beloy, M. Pizzocaro, C. W. Oates, and A. D. Ludlow, *Science* **341**, 1215 (2013).

- [13] A. D. Ludlow, *The Strontium Optical Lattice Clock: Optical Spectroscopy with Sub-Hertz Accuracy*, Ph.D. thesis, University of Colorado (2008).
- [14] W. M. Itano, J. C. Bergquist, J. J. Bollinger, J. M. Gilligan, D. J. Heinzen, F. L. Moore, M. G. Raizen, and D. J. Wineland, *Physical Review A* **5**, 3554 (1993).
- [15] G. Santarelli, P. Laurent, P. Lemonde, and A. Clairon, *Physical Review Letters* **82**, 4619 (1999).
- [16] T. L. Nicholson, M. J. Martin, J. R. Williams, B. J. Bloom, M. Bishof, M. D. Swallows, S. L. Campbell, and J. Ye, *Physical Review Letters* **109**, 230801 (2012).
- [17] M. Takamoto, F.-L. Hong, R. Higashi, and H. Katori, *Nature* **435**, 321 (2005).
- [18] F. Riehle, *Physics* **5**, 126 (2012).
- [19] M. A. Lombardi, T. P. Heavner, and S. R. Jefferts, *NCSL International Measure* **2**, 74 (2007).
- [20] J. Ye, H. J. Kimble, and H. Katori, *Science* **320**, 1734 (2008).
- [21] S. G. Porsev, A. D. Ludlow, M. M. Boyd, and J. Ye, *Phys. Rev. A* **78**, 032508 (2008).
- [22] R. H. Dicke, *Phys. Rev.* **89**, 472 (1953).
- [23] S. M. Foreman, *Femtosecond Frequency Combs for Optical Clocks and Timing Transfer*, Ph.D. thesis, University of Colorado (2007).
- [24] M. M. Boyd, T. Zelevinsky, A. D. Ludlow, S. Blatt, T. Zanon-Willette, S. M. Foreman, and J. Ye, *Phys. Rev. A* **76**, 022510 (2007).
- [25] G. K. Woodgate, *Elementary Atomic Structure*, 2nd ed. (Oxford University Press, New York, 1980).
- [26] A. Lurio, M. Mandel, and R. Novick, *Phys. Rev.* **126**, 1758 (1962).
- [27] C. J. Foot, *Atomic Physics*, 1st ed. (Oxford University Press, New York, 2011).
- [28] M. M. Boyd, T. Zelevinsky, A. D. Ludlow, S. M. Foreman, S. Blatt, T. Ido, and J. Ye, *Science* **314**, 1430 (2006).
- [29] M. S. Safronova, S. G. Porsev, U. I. Safronova, M. G. Kozlov, and C. W. Clark, *Phys. Rev. A* **87**, 012509 (2013).
- [30] S. G. Porsev and A. Derevianko, *Phys. Rev. A* **74**, 020502 (2006).
- [31] J. W. Farley and W. H. Wing, *Phys. Rev. A* **23**, 2397 (1981).
- [32] T. Middelmann, C. Lisdat, S. Falke, J. Winfred, F. Riehle, and U. Sterr, *Instrumentation and Measurement, IEEE Transactions on* **60**, 2550 (2011).
- [33] A. Derevianko and S. G. Porsev, in *Advances in Atomic, Molecular, and Optical Physics*, Vol. 60, edited by P. B. E. Arimondo and C. Lin (Academic Press, 2011) pp. 415 – 459.

- [34] R. Grimm, M. Weidemller, and Y. B. Ovchinnikov, in *Advances in Atomic, Molecular, and Optical Physics*, Vol. 42, edited by B. Bederson and H. Walther (Academic Press, 2000) pp. 95 – 170.
- [35] G. K. Campbell, A. D. Ludlow, S. Blatt, J. W. Thomsen, M. J. Martin, M. H. G. de Miranda, T. Zelevinsky, M. M. Boyd, J. Ye, S. A. Diddams, T. P. Heavner, T. E. Parker, and S. R. Jefferts, *Metrologia* **45**, 539 (2008).
- [36] R. Drever, J. Hall, F. Kowalski, J. Hough, G. Ford, A. Munley, and H. Ward, *Applied Physics B* **31**, 97 (1983).
- [37] M. Swallows, M. Martin, M. Bishof, C. Benko, Y. Lin, S. Blatt, A. Rey, and J. Ye, *Ultrasonics, Ferroelectrics and Frequency Control*, IEEE Transactions on **59**, 416 (2012).
- [38] M. Notcutt, L.-S. Ma, A. D. Ludlow, S. M. Foreman, J. Ye, and J. L. Hall, *Phys. Rev. A* **73**, 031804 (2006).
- [39] P. G. Westergaard, J. Lodewyck, L. Lorini, A. Lecallier, E. A. Burt, M. Zawada, J. Millo, and P. Lemonde, *Phys. Rev. Lett.* **106**, 210801 (2011).